Effect of reabsorption and photon recycling on photoluminescence spectra and transients in lead-halide perovskite crystals

JPhys Materials

PAPER

Effect of reabsorption and photon recycling on photoluminescence spectra and transients in lead-halide perovskite crystals

Florian Staub[1], **Irina Anusca**[2], **Doru C Lupascu**[2], **Uwe Rau**[1] **and Thomas Kirchartz**[1,3]

[1] IEK5-Photovoltaik, Forschungszentrum Jülich, D-52425 Jülich, Germany
[2] Institute for Materials Science and Center for Nanointegration Duisburg-Essen (CENIDE), University of Duisburg-Essen, Universitätsstraße 15, D-45141 Essen, Germany
[3] Faculty of Engineering and CENIDE, University of Duisburg-Essen, Carl-Benz-Str. 199, D-47057 Duisburg, Germany

E-mail: t.kirchartz@fz-juelich.de

Keywords: metal-halide perovskites, single crystals, photoluminescence, photon recycling

Supplementary material for this article is available online

OPEN ACCESS

RECEIVED
12 November 2019

REVISED
17 January 2020

ACCEPTED FOR PUBLICATION
24 January 2020

PUBLISHED
17 February 2020

Abstract

Explaining the time-dependent evolution of photoluminescence spectra of halide perovskite single crystals after pulsed excitation requires the consideration of a range of physical mechanisms, including electronic transport, recombination and reabsorption. The latter process of reabsorption and re-generation of electron-hole pairs from a photon created by radiative recombination in the single crystal itself is termed photon recycling and has been a highly controversial topic. We use photoluminescence experiments performed under different illumination conditions combined with numerical simulations that consider photon recycling to show which parameters affect temporal decays, spectral shifts and differences in the illumination direction. In addition, we use numerical simulations with and without photon recycling to understand the relative importance of charge-carrier transport and photon recycling. We conclude that under most relevant illumination conditions and times after the pulse, electronic transport is more important than photon recycling for the spectral behavior of the transients. However, inclusion of photon recycling is imperative for the understanding of the absolute density of electrons and holes present in the crystal during a certain time after the pulse.

1. Introduction

Over the last years, lead-halide perovskite thin films have been studied extensively for applications in photovoltaic [1–5] and light emitting devices [6–11] due to their unique defect tolerance [12, 13], high absorption coefficients [14] and long charge carrier lifetimes [15, 16]. Lead-halide perovskites are interesting not only for practical applications but also as a model system for a bulk semiconductor operating close to the radiative limit, i.e. the situation where recombination is predominantly radiative in nature [17]. Approaching the radiative limit was so far only possible in III–V materials [18–21] or in low conductivity quantum dot films [22] but not in solution-processed, three dimensional semiconductors. Better understanding the fundamental reasons for the observed properties of halide perovskites would therefore be highly valuable [23, 24]. While polycrystalline thin films are highly application relevant, their properties vary strongly with the preparation conditions and their crystallinity with lateral variations having been shown to strongly affect device performance [25–27]. Thus, single crystals [28–31] made from lead-halide perovskites have received considerable attention as a grain-boundary-free model system [28, 32] for the material class. In addition, there are some applications where single crystals have intrinsic advantages such as γ-ray [33] and x-ray detectors [34, 35], photodetectors [36] and gas sensors [29]. In addition, also efforts to make single crystal perovskite solar cells are pursued [37, 38] with a recent report of efficiencies exceeding 20% [38]. Close to the radiative limit, physical phenomena such as photon recycling [23, 39, 40] become important that are not or hardly relevant for most materials used in photovoltaics. Photon recycling specifies the process of photogeneration of electron-hole pairs by photons that are created by radiative recombination of electron-hole pairs. Thus, photon recycling considers that a sample

might illuminate itself if in non-equilibrium. Note that photon recycling requires reabsorption to happen but while reabsorption is a phenomenon happening even in samples with low luminescence yield, for the whole chain of processes involved in photon recycling to happen, radiative recombination has to be a likely event [41]. Photon recycling has been invoked to affect various aspects of luminescence based experiments performed on halide perovskite samples. Examples are the interpretation of bimolecular recombination in photoluminescence transients on thin films [42, 43], the lateral decay of luminescence away from an excitation spot in thin films [44, 45] or the redshift of transient photoluminescence spectra with time [31]. In addition, efficient photon recycling and suppression of parasitic absorption can affect the performance of perovskite solar cells, photodetectors or light emitting devices by increasing the diffusion lengths [46] of charge carriers and by increasing their concentration and thereby the open-circuit voltage of a photovoltaic device [47]. While it is rather undisputed that photon recycling exists and affects experimental data [17, 42, 43, 45, 48] and device performance [47, 49, 50], the relative importance of the effect is highly disputed with statements ranging from the conclusion that photon recycling as a carrier transport phenomenon is negligible [51] to dominant [52].

In order to study photon and electron transport in halide-perovskites, we use lead-bromide based single crystals as a model system and combine time-resolved photoluminescence measurements with simulations that allow us to switch on or off the effect of photon recycling and to understand the influence of parameters describing transport and recombination on the PL transients. Our model of charge-carrier dynamics in the perovskite crystal accounts for the interplay of all relevant charge-carrier processes at once: the model includes radiative and non-radiative charge-carrier recombination in the bulk, recombination via defects at the crystal surface, and charge-carrier transport by diffusion as well as photon recycling. By comparing the results of the model with experimental PL data, in particular the spectral shape of the PL and the change of that shape as a function of delay time after the laser pulse, we identify the processes that affect our data. We find that by combining different measurement modes and by fitting the model to the experimental data, we can determine the recombination velocities of both interfaces (front and back). From analyzing the experimentally observed change of the spectral shape of the photoluminescence as a function of delay time with our numerical model, we can estimate charge-carrier mobilities. From the simulations as well as from simple analytical estimates we can finally identify whether electronic or optical transport (i.e. photon recycling) is dominant. We find that both mechanisms are of similar importance with the excitation density determining the exact ratio of the two. Generally, photon recycling has a stronger impact on the total concentration of charge carriers rather than on the fundamental behavior of the spectra as a function of time. This finding implies that conflicting observations [51, 52] in literature can possibly be rationalized by understanding that electronic and optical diffusion are both similarly efficient and depending on the exact design of experiment either may appear to be more important.

2. Results

2.1. Photoluminescence measurement configuration

In the following, we measure time-resolved and photon-energy resolved photoluminescence (tr-PL) of a $CH_3NH_3PbBr_3$ single crystal in two different measurement configurations as illustrated in figure 1. In the first configuration, the single crystal is illuminated by the excitation pulse from the front side (fsi), from which luminescence is also detected by the gated camera. Due to a high absorption coefficient α at the photon energy E of the excitation source, charge carriers and, subsequently, photoluminescence are mainly generated in close proximity to the sample surface. Therefore, the luminescence has to pass only through marginal segments of the entire crystal before it can be coupled out of the front side of the sample and detected in this configuration. Upon back-side illumination (bsi) on the other side, luminescence is detected in transmission mode. Especially in this configuration, detected luminescence has to traverse the entire thickness while the crystal basically acts like a filter for its own luminescence. Therefore, different photoluminescence spectra in terms of shape, peak position and intensity but also differences in the temporal changes of the mentioned properties can be expected for the two measurement configurations.

2.2. Photoluminescence spectra

Figure 2(a) shows the initial normalized photoluminescence spectra of a 1.7 mm thick $CH_3NH_3PbBr_3$ crystal upon front (blue spheres) and back side illumination (red spheres). Due to severe reabsorption of photoluminescence, the high energy part (i.e. where the absorption coefficient α shown in figure 2(b) is sufficiently high) of the spectrum recorded upon back side illumination is abruptly cut off. Thus, the corresponding peak shows a significant red shift of ~150 meV. The experimental data shown in symbols in figure 2(a) are compared with numerical simulations shown in solid lines that fit the experimental data reasonably well. These simulations are based on an extension of a photon recycling code that was originally presented and discussed by Mattheis [53, 54]. For the present purpose of simulating thick crystals, we had to

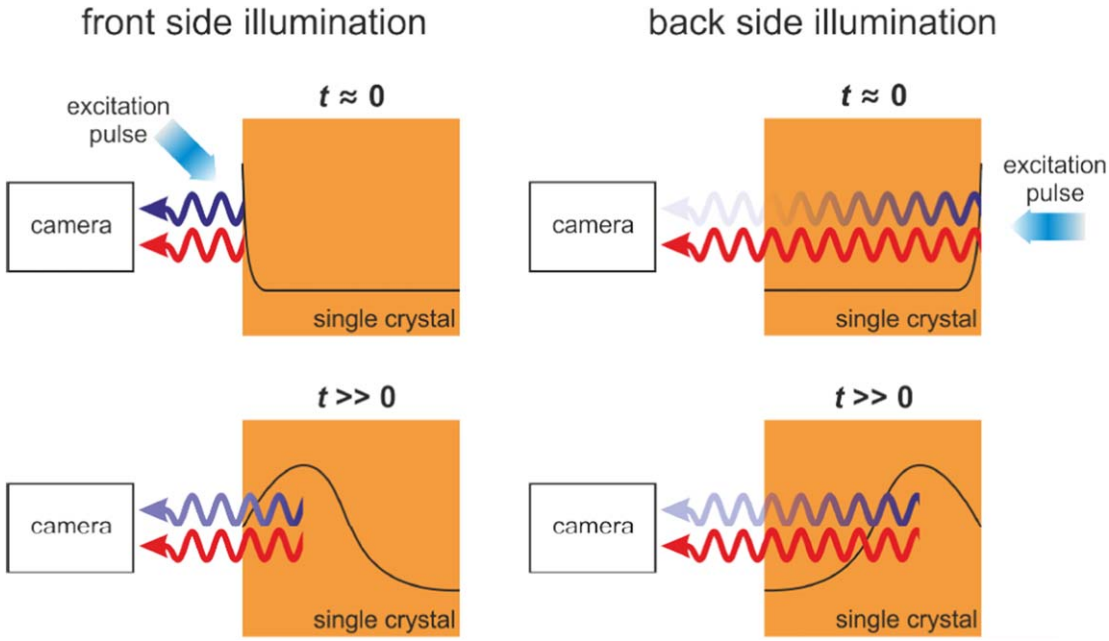

Figure 1. Overview of the used measurement configurations. Front side illumination (left) specifies the situation where illumination and detection of luminescence are done from the same side (here the left side) while back side illumination (right) specifies the situation where illumination and detection are done from different sides. In the back-side illumination configuration the effect of reabsorption and photon recycling is substantially amplified relative to the front side illumination case.

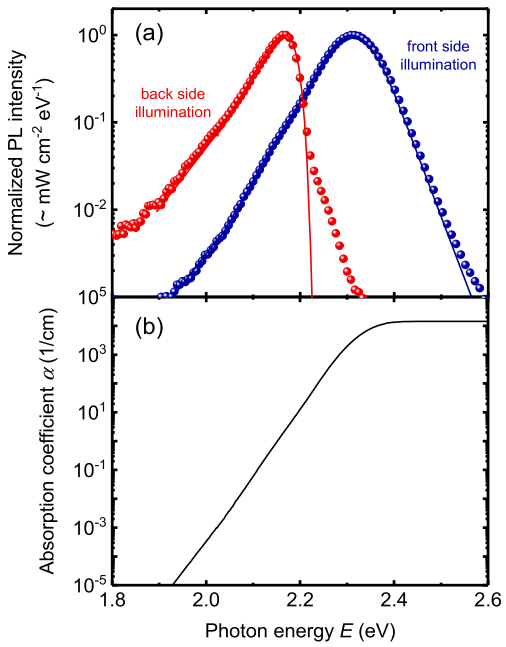

Figure 2. Comparison of PL spectra for front and back side illumination. (a) Initial photoluminescence spectra of a $CH_3NH_3PbBr_3$ single crystal, which is excited with a photon density of $\phi = 2.9 \times 10^{14}$ cm^{-2} and a photon energy $E = 3.07$ eV. Here, the spectra (spheres) are recorded in two different measurement configurations (see also figure 1), denoted as front side illumination (blue) and back side illumination (red). Additionally, simulated spectra are shown as solid lines. (b) Absorption coefficient of the single crystals determined from modeling the photoluminescence spectra shown in panel (a).

adapt the mesh to allow for a treatment of length-scales from nm to mm. The code considers optical generation assuming a Lambert-Beer like absorption profile of the laser generating the electron hole pairs initially. In time, the laser pulse is assumed to have a Gaussian profile with a full width at half maximum of 2 ns. The peak of the Gaussian defines the zero on the time axis. Transport is simulated assuming a field-free crystal with diffusion as the only electronic transport mechanism and photon recycling as an optical mechanism of charge redistribution. We assume that every grid-point in our one-dimensional grid may emit photons based on the

Table 1. Transport and recombination parameters applied and derived from modeling transient photoluminescence data of a $CH_3NH_3PbBr_3$ perovskite single crystal.

Parameter	Symbol	Value	Sensitive mostly to which part of the experiment?
Auger recombination coefficient	C	$5.0\,(\pm 2) \times 10^{-28}\,\mathrm{cm^6\,s^{-1}}$	Absolute decay at early times and high fluences (see figure S1)
Radiative recombination coefficient	k_{rad}	$5.5\,(\pm 1.5) \times 10^{-11}\,\mathrm{cm^3\,s^{-1}}$	Absolute decay at early times and high fluences (figure S1)
Bulk Shockley–Read–Hall lifetime	τ_{SRH}	$2.5\,(\pm 0.7)\,\mu\mathrm{s}$	Absolute decay at longer times and lower fluences
Charge carrier mobility	μ	$15\,(\pm 10)\,\mathrm{cm^2\,V^{-1}\,s^{-1}}$	PL peak position as a function of time for front-side illumination (see figure 7)
Front surface recombination velocity	S_f	$6700\,(\pm 1300)\,\mathrm{cm\,s^{-1}}$	Absolute decay for front-side illumination
Back surface recombination velocity	S_b	$1100\,(\pm 300)\,\mathrm{cm\,s^{-1}}$	Absolute decay for back-side illumination
Crystal thickness	d	$1.7\,(\pm 0.1)\,\mathrm{mm}$	Measured

concentrations of electron-hole pairs that are then emitted in a spherical angle of 4π. These photons may then be reabsorbed within the crystal, be emitted from one of the two surfaces or be reflected internally. The internal generation rate is calculated assuming up to 100 reflections before the remaining photons (not absorbed or emitted after 100 reflections) are truncated.

We assume recombination to consist of non-radiative bulk and surface recombination as well as radiative bulk recombination. The bulk recombination rate R_b is

$$R_b = R_{rad} + R_{SRH} + R_{Aug} = k_{rad}np + \frac{np}{(n+p)\tau_{SRH}} + C(n+p)np, \tag{1}$$

where R_{rad} is the radiative recombination rate, k_{rad} the radiative recombination coefficient, n and p are the electron and hole concentrations, R_{SRH} is the Shockley–Read–Hall recombination rate and τ_{SRH} is the Shockley–Read–Hall lifetime which is assumed to be the same for electrons and holes for simplicity. The last term R_{Aug} represents Auger recombination with the Auger coefficient C. At the surfaces, we use the boundary conditions

$$\pm D_n \frac{dn}{dx}\bigg|_{x=0,d} = S_{f,b}\Delta n \tag{2}$$

for electrons and

$$\pm D_p \frac{dp}{dx}\bigg|_{x=0,d} = S_{f,b}\Delta p \tag{3}$$

for holes. Here, $S_{f,b}$ is the surface recombination velocity at the front (f) or back (b) side of the crystal and D_n, D_p are the diffusion constants for electrons and holes. The diffusion constants are in general related to the charge carrier mobilities $\mu_{n/p}$ via $D_{n/p} = \mu_{n/p}\,kT/q$, where kT/q is the thermal voltage (~25.8 mV at room temperature). Here, we also assume the mobilities to be the same for electrons and holes. The surface recombination velocities, We assume the surface recombination velocities to be different between front and back surface but to be always the same for electrons and holes, we then adjust the parameters of the model until it reproduces the experimental spectra for fsi and bsi. We take care to reproduce both the information about the transient decay as well as the spectral shift of the luminescence seen in the fsi configuration. Once we obtain a parameter set that reproduces all experimental data, we study the sensitivity of the fit to variations in the different parameters. Table 1 presents the parameters that reproduce the experiments most closely and that are used for the simulations in the paper except otherwise noted. In addition, for every parameter a range is given that still leads to reasonable fits, while leaving the given range leads to substantial deviations from the experimental data. In addition, table 1 gives explanations for why the time dependent photoluminescence spectra obtained experimentally in this work are sensitive to these parameters.

2.3. Spectral shifts with decay time

The spectral shift between front and back side illumination shown in figure 2(a) can be easily explained by a simple reabsorption effect, caused by the large thickness of the crystal relative to the absorption length of photons. However, the spectral shifts with time shown in figures 3(a) and (b) are substantially less straightforward to explain. We note that in case of front-side illumination (figure 3(a)), there is a substantial shift in the spectrum at early times and after 100 ns. However, in case of bsi, this spectral shift is absent. The two curves at early times and at 100 ns after the pulse basically coincide. While the simulations shown in lines also reproduce that same behavior, it is not immediately intuitive that front and back side illumination behave differently in

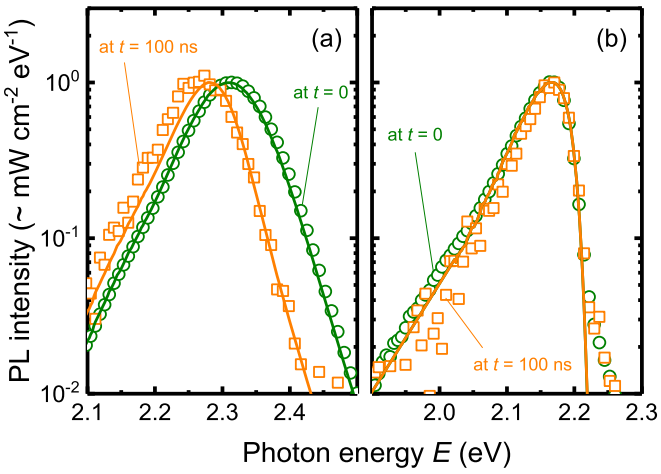

Figure 3. Spectral shift versus time for front side and back side illumination. Normalized measured photoluminescence spectra at delay times of $t = 0$ (circles) and $t = 100$ ns (squares) upon (a) front side illumination and (b) back side illumination with a photon density of 2.9×10^{14} cm^{-2} each. Solid lines represent simulated spectra.

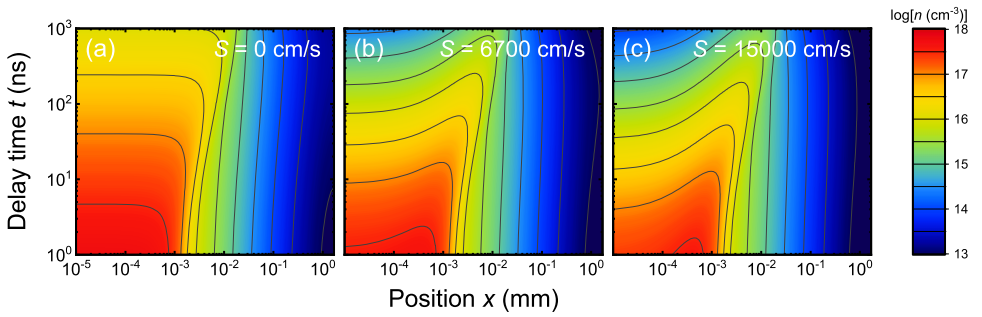

Figure 4. Movement of the charge carrier front away from the front surface. Comparison of simulated charge carrier profiles $n(x, t)$ within a perovskite single crystal for different surface recombination velocities: (a) $S = 0$ cm s^{-1}, (b) $S = 6700$ cm s^{-1} and (c) $S = 15\,000$ cm s^{-1}. All simulations were carried out for a charge carrier mobility of $\mu = 15$ cm^2 V^{-1} s^{-1}. The higher S is, the more distinctly a peak in $n(x, t)$ is formed that moves away from the front surface at $x = 0$ with time. Note that S represents here both S_f and S_b but only S_f is relevant for the results.

terms of their spectral shifts with delay time (see also figures S1 and S2 is available online at stacks.iop.org/JPMATER/3/025003/mmedia for the complete PL transients). In order to understand this phenomenon, let us first have a look at how the charge-carrier concentrations in our simulations change as a function of time after the pulse.

Figures 4(a)–(c) shows a series of colorplots where the electron concentration is plotted as a function of delay time and position and from (a) to (c) for three different surface recombination velocities S at the front surface (front side illumination assumed). In the absence of surface recombination (panel (a)), the carrier concentration moves deeper into the crystal with delay time but always stays highest close to the front contact, where most of the charge generation took place. With increasing values of S (panels (b) and (c)), a clear peak of the electron concentration develops that moves further away from the front surface with longer times. Close to the front surface, the electron concentration is substantially lower than deeper in the bulk, because recombination is high. The position of the maximum electron concentration will determine the amount of reabsorption that the emitted luminescence encounters on its way to the front surface and therefore the spectral position of the detected luminescence. Thus, we note that the spectrum in front side illumination should indeed depend on the time after the pulse and in addition, it should depend on the front surface recombination velocity.

To understand the phenomenon in a slightly more quantitative way, let us now assume for the moment that we are in the case of high S and, therefore, we can assume that luminescence originates from a small volume inside the crystal that moves away from the front surface with time. The rate of spontaneous emission caused by radiative recombination in a semiconductor is directly connected by detailed balance to the rate of photon absorption (van Roosbroeck–Shockley equation [55]). Hence, in the case of luminescence originating from a small volume it will be proportional to [56].

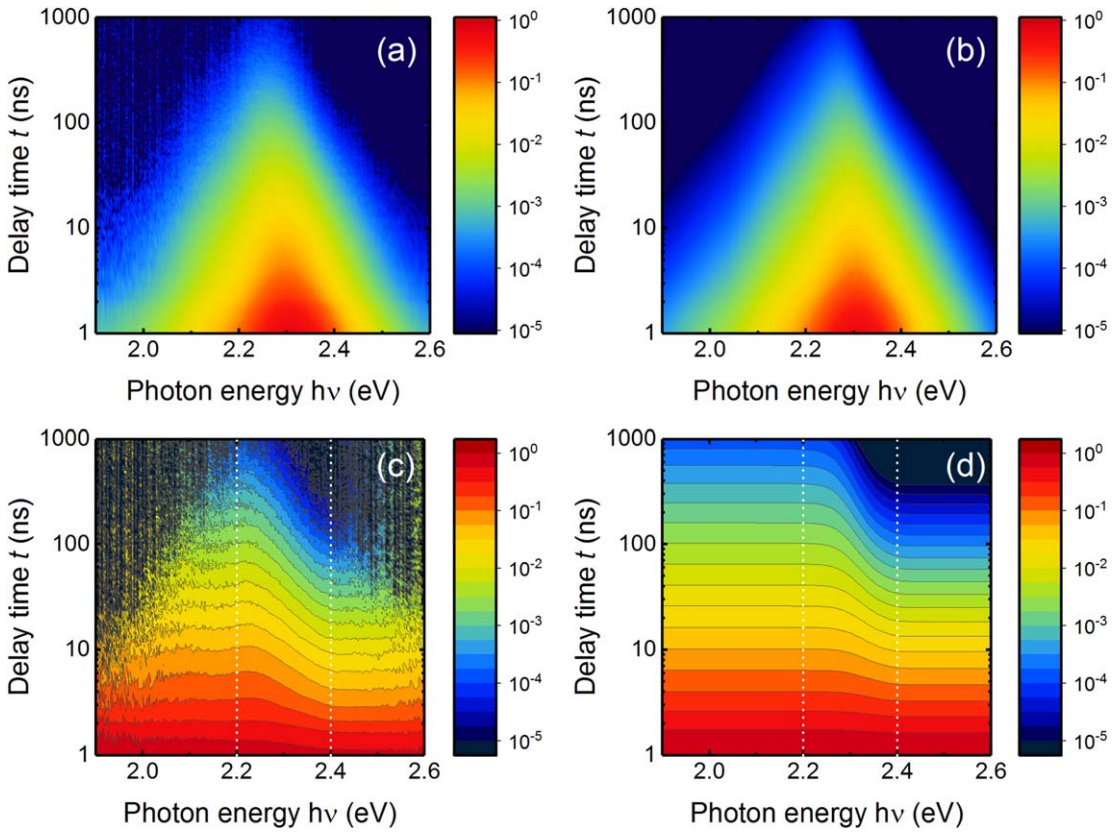

Figure 5. Comparison of measured and simulated spectrally resolved photoluminescence decays of a $CH_3NH_3PbBr_3$ single crystal in front side illumination. (a) Shows the experimental data normalized to the maximum value as a function of time and energy. (b) shows the equivalent simulated data. (c) Shows the experimental data normalized to maximum values at $t = 0$ (for each energy individually) and (d) the equivalently presented simulation data. A clear spectral shift of the peak is visible in experiment and simulation. The shift can be best seen in panels (c) and (d) that show that higher energy features of the spectrum are decaying faster than lower energy features.

$$\phi_{\mathrm{fsi}}(E,\,t) \propto \alpha(E)\phi_{\mathrm{bb}}(E)\exp\left(-\alpha(E)x(t)\right), \tag{4}$$

where $x(t)$ is the position of the emitting plane as a function of delay time t and ϕ_{bb} is the black body spectrum per area, time and energy interval given by

$$\phi_{\mathrm{bb}}(E) = \frac{2E^2}{h^3c^2}\frac{1}{\exp\left(\dfrac{E}{kT}\right)}, \tag{5}$$

where h is Planck's constant and c is the speed of light. Here, the term $\exp\left(-\alpha(E)x(t)\right)$ represents the effect of reabsorption of light that has to travel (at least) the distance x to leave the sample through the front surface. In case of back side illumination, the emitting plane would start at roughly the crystal thickness d at early times after the laser pulse and move towards the observing detector over time. Thus, the luminescence follows as

$$\phi_{\mathrm{bsi}}(E,\,t) \propto \alpha(E)\phi_{\mathrm{bb}}(E)\exp\left(-\alpha(E)[d - x(t)]\right). \tag{6}$$

We note that the two situations differ in that both should feature spectral shifts but the shift under front-side illumination dampens the high energy (=high α) part of the spectrum, in consequence leading to the red shift with time observed in figure 3(a). In contrast bsi leads to an amplification of the high energy part of the spectrum, while for low values of alpha (low photon energies), the spectrum is multiplied with values close to $\exp(0) = 1$. The high energy part of the spectrum, however, is filtered out completely by the thick crystal. Thus, the region where a spectral change would be expected is experimentally not visible in back side illumination.

To illustrate this observation, figures 5 and 6 show the measured and simulated spectra under front (figure 5) and back (figure 6) side illumination. These spectra are normalized in (a) and (b) to the highest point of the spectrum at the shortest delay time and in (c) and (d) to the (whole) spectrum at shortest delay time, which serves to better observe spectral changes. Figure 5 shows the expected spectral changes for fsi that are due to the increased reabsorption caused by charge carriers diffusing deeper into the crystal. Figure 6, however, shows the situation for bsi, where the PL peak does not shift in the experiment. In the simulation, a strong amplification of

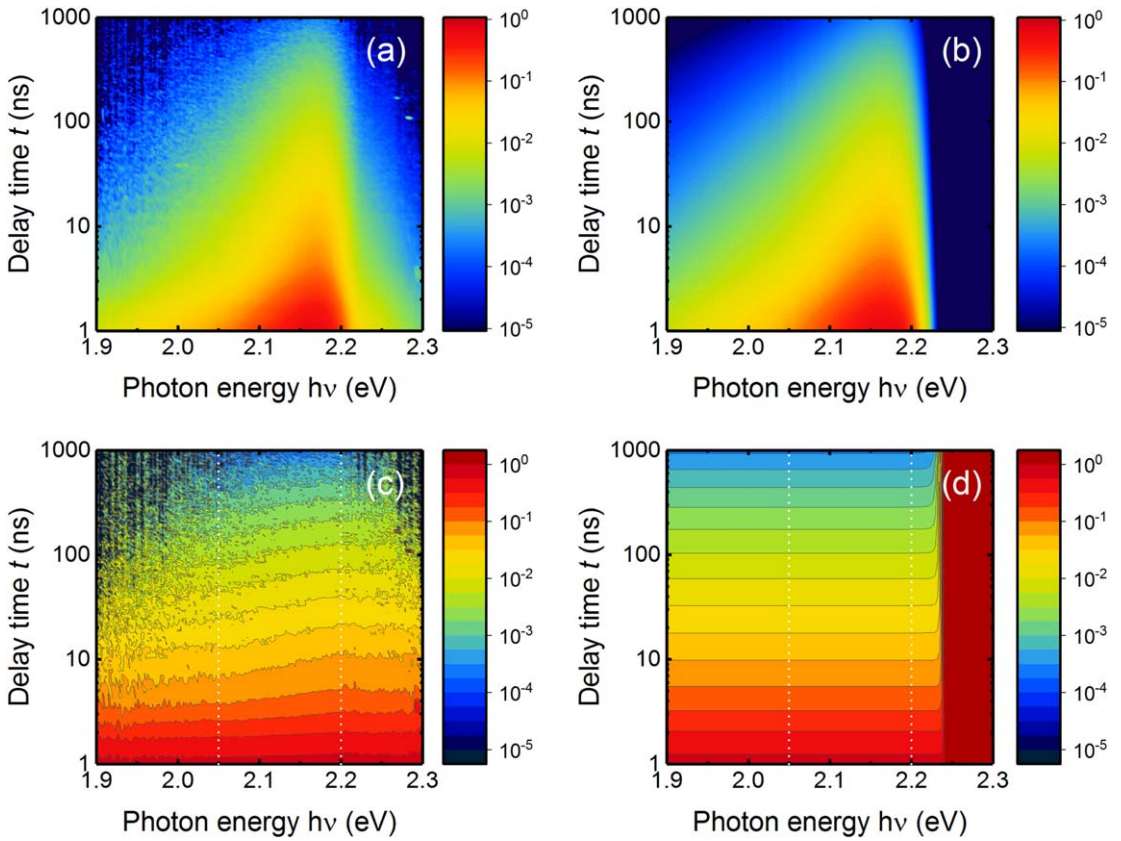

Figure 6. Comparison of measured and simulated spectrally resolved photoluminescence decays of a $CH_3NH_3PbBr_3$ single crystal in back side illumination. (a) Shows the experimental data normalized to the maximum value as a function of time and energy. (b) shows the equivalent simulated data. (c) Shows the experimental data normalized to maximum values at $t = 0$ (for each energy individually) and (d) the equivalently presented simulation data. The spectral shape of the PL hardly changes with delay time for bsi. A delay would be expected for high energies (see panel (d)), however, in experiment the higher energy photons are completely blocked by reabsorption and in practice therefore no shift is visible.

luminescence is predicted in the high energy tail of the spectrum (dark red region in figure 6(d)). However, this amplification is invisible in panel (b), because the luminescence is already extremely low in this region.

2.4. Determination of mobility and surface recombination velocity

Based on the movement of the charge-carrier front shown in figure 4, we can understand how in fsi the peak of the PL emission will shift as a function of time. This movement will depend on the mobility of the charge carriers. In addition, the sharpness of the charge-carrier front will depend on the surface recombination velocity at the front of the crystal. A low surface recombination velocity will create a broad region of high charge-carrier concentration (figure 4(a)) while a high surface recombination velocity will create a sharp peak of the charge-carrier concentration that moves over time. Depending on mobility and surface recombination velocity, the time-dependent spectral shift will therefore change, which allows us in turn to estimate those parameters from our experimental data. Figure 5 presents the experimental data (panels (a) and (c)) and the simulated data using the parameters in table 1. While figure 5 already indicates that the simulation reproduces key features of the experimental data quite well, it is not immediately obvious how sensitive the fit is to the surface recombination velocity and the mobility of the charge carriers.

In order to better understand the sensitivity of the spectral shift to these parameters, figure 7(a) shows how the simulated peak position (x-axis) changes as a function of mobility (y-axis) for different times after the pulse (see also figures S3–S7 for additional simulation data). Note that $t = 0$ ns is during the pulse which is assumed to have a Gaussian shape in time at which time diffusion of charge carriers has already started and may also lead to shifts if the mobility is assumed to be >1000 cm^2 V^{-1} s^{-1}. The key information of figure 7(a) is however that the spectrum would always shift over time but how much it shifts strongly depends on the mobility. This dependence on mobility is much stronger than the dependence of the spectral shift on surface recombination velocity as shown in figure 7(b). However, the surface recombination velocity has a strong impact on the decay of the total luminescence (see figure S8) which allows us to disentangle the influence of mobility and surface

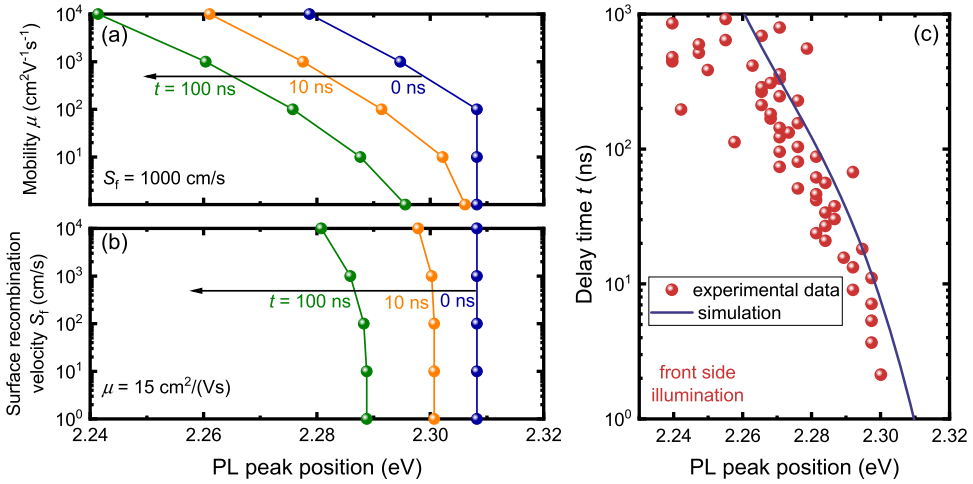

Figure 7. Time-dependent spectral shifts of the PL peak for front-side illumination. Simulated photoluminescence peaks as a function of (a) mobility and (b) surface recombination velocity for three times after the laser pulse (0, 10, and 100 ns). In panel (a), the surface recombination velocity was kept constant at $S_f = 1000$ cm s^{-1} and in panel (b), the mobility was kept constant at $\mu = 15$ cm^2 V^{-1} s^{-1}. As seen in (a), the peak shift is highly sensitive to the mobility, because the value of the mobility determines the speed of the movement of the carrier front seen in figure 4. The surface recombination velocity determines the sharpness of the carrier front but not the speed of its movement and, hence, the PL peak still shifts with time but it does not change substantially with the value of the surface recombination velocity. (c) PL peak position as a function of delay time showing experimental data (symbols) and simulation data (line) using a value of $S_f = 6700$ cm s^{-1} and $\mu = 15$ cm^2 V^{-1} s^{-1}.

recombination velocity. Figure 7(c) shows the experimental and simulated shift of the PL peak with delay time for comparison. The parameters that best fit to the data are $S_f = 6700$ cm s^{-1} and $\mu = 15$ cm^2 V^{-1} s^{-1}.

2.5. Photon recycling

The reason for the time-dependent shift of the PL spectra for front side illumination shown in figure 3(a) is the propagation of charge carriers into the bulk over time as seen in figure 4 (simulated charge-carrier concentration n as a function of space and time) mainly due to charge-carrier diffusion. So far, we have always included photon recycling in the simulation of our data. However, we did not specifically discuss how much the simulations and explanations would change if we could switch off photon recycling, which is possible in simulation but not in experiment. Before we study numerical simulations for that purpose, we will first analytically estimate the relative influence of electrical diffusion and photon recycling to transport charge carriers and thereby smoothen out spatially inhomogeneous charge carrier profiles. For this purpose, we introduce a self-absorption length L_{PR}, defined as the mean distance between the point of radiative recombination and that of reabsorption which is mathematically expressed via

$$L_{PR} = \frac{\int_0^{2\pi} d\varphi \int_0^{\frac{\pi}{2}} \sin(\theta)\cos(\theta) d\theta \int_0^{\infty} \alpha(E)\phi_{bb}(E) dE}{2\pi \int_0^{\infty} \alpha^2(E)\phi_{bb}(E) dE}$$
$$= \frac{\int_0^{\infty} \alpha(E)\phi_{bb}(E) dE}{2\int_0^{\infty} \alpha^2(E)\phi_{bb}(E) dE} \approx 1.1\ \mu\text{m}. \quad (7)$$

Using the absorption coefficient shown in figure 2(b), we find a self-absorption length of 1.1 μm, which is three orders of magnitude smaller than the crystal dimensions. Thus, relative to the crystal size, photon recycling transports charge over small distances. Assuming a mobility of 15 cm^2 V^{-1} s^{-1}, a charge carrier would cover a distance of 1.1 μm in about 30 ns by diffusion. If we consider that the radiative recombination coefficient is $k_{rad} = 5.5 \times 10^{-11}$ cm^3 s^{-1}, we find that the radiative lifetime $\tau_{rad} = (k_{rad} n)^{-1}$ is shorter than 30 ns if $n > 6 \times 10^{17}$ cm^{-3}. Thus, based on this simple calculation, we find that photon recycling should be the more efficient transport mechanism for $n > 6 \times 10^{17}$ cm^{-3} while for lower carrier concentrations, diffusion should be more efficient. For the excitation density of 2.9×10^{14} photons/cm^2 used for most of the experiments and the simulations, and using the simulation parameters shown in table 1, the electron concentration drops below 6×10^{17} cm^{-3} after 3 ns due to surface recombination, Auger recombination and radiative recombination. Thus, diffusion is the dominant charge transport mechanism for all but very short times using the parameters shown here. However, note that this does not imply that photon recycling is not important or irrelevant to

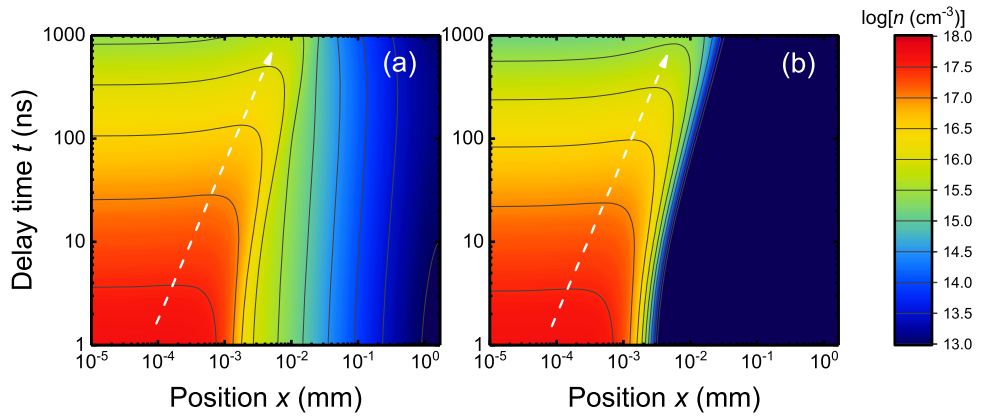

Figure 8. Simulations of charge carrier profiles with and without photon recycling. Simulated charge-carrier densities $n(x, t)$ within a perovskite single crystal as a function of time. While panel (a) includes photon recycling, panel (b) neglects reabsorption but apart from that applies the same recombination conditions as in panel (a).

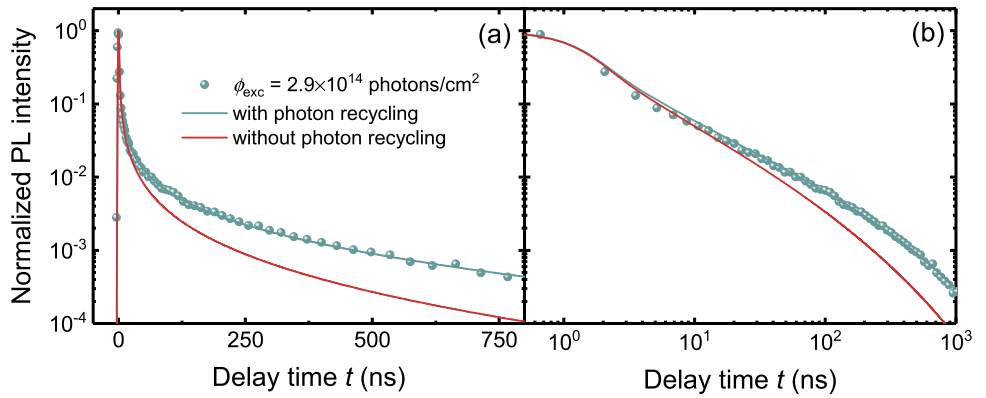

Figure 9. Comparison of the effect of photon recycling on the PL transients. Normalized photoluminescence transients simulated with (green) and without (red) the effect of photon recycling are compared with experimental data (spheres) under back side illumination. Panel (a) shows the same data as in panel (b) but on a double-logarithmic scale.

accurately model and reproduce the experimental data. This is due to the fact that photon recycling has two functions. It smoothens inhomogeneous carrier concentrations that are created by optical excitation at a wavelength where light absorption happens predominantly at the front surface of the crystal. In addition, photon recycling increases the carrier concentration in the vicinity of the emission spot.

Figure 8 illustrates this finding by showing in panel (a) the carrier concentration including and in panel (b) excluding the effect of photon recycling. The latter means that the term due to internal generation by absorption of photons generated by radiative recombination is omitted from the calculation. We find from figure 8 that the temporal trend of the charge-carrier front indicated by the white arrow (region of highest electron concentration) is basically unchanged between panels (a) and (b). With photon recycling, the carrier concentration decays more smoothly towards larger distances away from the front surface. However, these regions do not contribute substantially to the total photoluminescence.

Figure 9 shows the measured photoluminescence transients for bsi (spheres) compared with a simulation using the parameters in table 1 (solid blue line) and a simulation with the same parameters but without photon recycling (solid red line). We note that not considering photon recycling leads to a faster decay, which would have to be compensated by a smaller value of k_{rad} in a similar way as has previously been observed for thin films.

3. Conclusions

In conclusion, we have presented a combined numerical-experimental study of photoluminescence in halide perovskite single crystals. We use two different measurement modes, front side and back side illumination, that differ in their photoluminescence spectra and the way these spectra change over time. We quantitatively explain our observations by a combination of reabsorption effects and surface recombination. We explain how

information on the recombination velocity at both front and back interface as well as on the mobility follows from a careful examination of the spectral shifts and transient decays of the absolute PL intensity. Finally, we discuss the effect of photon recycling which modifies the shape of the charge-carrier profile but shows minor impact on the progression of the charge-carrier front, which is identified as the main contributor to the overall photoluminescence intensity. Spectral changes observed during the photoluminescence measurements are primarily due to charge-carrier diffusion. It is apparent from simulations that also in single crystals photon recycling partly counteracts the annihilation of charge carriers locally. Therefore, when it comes to quantitatively investigating and understanding the working mechanisms of single crystal devices, photon recycling has to be included.

4. Experimental section

4.1. Materials

4.1.1. Single crystal synthesis

$CH_3NH_3PbBr_3$ single crystals were synthesized in two steps according to the procedure reported by Im *et al* [57]. with small modifications. The precursors CH_3NH_3Br were synthesized by the reaction of stoichiometric amounts of methylamine, $CH_3–NH_2$, solution (33 wt% in absolute ethanol, Sigma Aldrich) and the corresponding halogen acid, HBr (48 wt% in H_2O) (Sigma Aldrich), under stirring in an ice bath for 3 h. The solvent was subsequently removed under vacuum in a rotary evaporator. The resulting salts were washed with absolute ethanol and absolute diethyl ether several times and finally dried in a vacuum oven at 60 °C for 12 h. In a second step, the synthesized salts CH_3NH_3Br were mixed with $PbBr_2$ (Sigma Aldrich) in molar ratios 1:1 in N, N-dimethylformamide (Acros Organics) at room temperature overnight. After vacuum evaporation of the solvents, we obtain the crystals. The crystals have been stored in a N_2 filled glovebox.

4.1.2. Transient photoluminescence measurements

Time-resolved photoluminescence (tr-PL) measurements were performed on samples under inert nitrogen atmosphere. The perovskite crystal was illuminated with 404 nm light pulses (~2 ns FWHM) originating from a Nitrogen-laser pumped dye laser. The laser system is the MNL 200 system from Lasertechnik Berlin and the pump laser emits a wavelength of 337.1 nm with a 20 Hz repetition rate. The dye used to obtain 404 nm pulses is Diphenylstilbene. The measurements are performed in the so-called front side and back side configuration (see figure 1). Photon densities were varied by the use of neutral density filters and applied as (2.9×10^{14}, 3.1×10^{13} and 1.4×10^{12}) photons/cm^2. The photoluminescence signal was spectrally resolved by a Spex 270m monochromator from Horiba Jobin Yvon and detected by a gated ICCD camera (iStar DH720 from Andor Solis). The width of the gate pulse, which keeps the multichannel gate open for the PL-related signal to impinge on the Si-detector, was 2 ns. The temporal resolution of the gate pulse delay is indicated as 25 ps.

Acknowledgments

T K and U R acknowledge the Helmholtz Association for funding via the PEROSEED project. I A and D C L acknowledge funding by the European Union and the state of Nordrhein-Westfalen through the project PeroBOOST (EFRE-0800120; NW-1-1-040h).

ORCID iDs

Doru C Lupascu https://orcid.org/0000-0002-6895-1334
Thomas Kirchartz https://orcid.org/0000-0002-6954-8213

References

[1] Jeon N J, Na H, Jung E H, Yang T Y, Lee Y G, Kim G, Shin H W, Il Seok S, Lee J and Seo J 2018 A fluorene-terminated hole-transporting material for highly efficient and stable perovskite solar cells *Nat. Energy* **3** 682–9
[2] Yang W S *et al* 2017 Iodide management in formamidinium-lead-halide-based perovskite layers for efficient solar cells *Science* **356** 1376
[3] Luo D *et al* 2018 Enhanced photovoltage for inverted planar heterojunction perovskite solar cells *Science* **360** 1442
[4] Jung E H, Jeon N J, Park E Y, Moon C S, Shin T J, Yang T Y, Noh J H and Seo J 2019 Efficient, stable and scalable perovskite solar cells using poly(3-hexylthiophene) *Nature* **567** 511–5
[5] Jiang Q, Zhao Y, Zhang X, Yang X, Chen Y, Chu Z, Ye Q, Li X, Yin Z and You J 2019 Surface passivation of perovskite film for efficient solar cells *Nat. Photon.* **13** 460–6
[6] Ban M *et al* 2018 Solution-processed perovskite light emitting diodes with efficiency exceeding 15% through additive-controlled nanostructure tailoring *Nat. Commun.* **9** 3892

[7] Yang X, Zhang X, Deng J, Chu Z, Jiang Q, Meng J, Wang P, Zhang L, Yin Z and You J 2018 Efficient green light-emitting diodes based on quasi-two-dimensional composition and phase engineered perovskite with surface passivation *Nat. Commun.* **9** 570
[8] Cho H *et al* 2015 Overcoming the electroluminescence efficiency limitations of perovskite light-emitting diodes *Science* **350** 1222–5
[9] Tan Z K *et al* 2014 Bright light-emitting diodes based on organometal halide perovskite *Nat. Nano* **9** 687–92
[10] Lin K *et al* , 2018 Perovskite light-emitting diodes with external quantum efficiency exceeding 20 percent *Nature* **562** 245–8
[11] Xu W *et al* 2019 Rational molecular passivation for high-performance perovskite light-emitting diodes *Nat. Photon.* **13** 418–24
[12] Brandt R E *et al* 2017 Searching for defect-tolerant photovoltaic materials: combined theoretical and experimental screening *Chem. Mater.* **29** 4667–74
[13] Brandt R E, Stevanoviç V, Ginley D S and Buonassisi T 2015 Identifying defect-tolerant semiconductors with high minority-carrier lifetimes: beyond hybrid lead halide perovskites *MRS Commun.* **5** 265–75
[14] De Wolf S, Holovsky J, Moon S J, Löper P, Niesen B, Ledinsky M, Haug F J, Yum J H and Ballif C 2014 Organometallic halide perovskites: sharp optical absorption edge and its relation to photovoltaic performance *J. Phys. Chem. Lett.* **5** 1035–9
[15] deQuilettes D W, Koch S, Burke S, Paranji R K, Shropshire A J, Ziffer M E and Ginger D S 2016 Photoluminescence lifetimes exceeding 8 μs and quantum yields exceeding 30% in hybrid perovskite thin films by ligand passivation *ACS Energy Lett.* **1** 438–44
[16] Liu Z *et al* 2019 Open-circuit voltages exceeding 1.26 V in planar methylammonium lead iodide perovskite solar cells *ACS Energy Lett.* **4** 110–7
[17] Braly I L, deQuilettes D W, Pazos-Outon L M, Burke S, Ziffer M E, Ginger D S and Hillhouse H W 2018 Hybrid perovskite films approaching the radiative limit with over 90% photoluminescence quantum efficiency *Nat. Photon.* **12** 355–61
[18] Miller O D, Yablonovitch E and Kurtz S R 2012 Strong internal and external luminescence as solar cells approach the Shockley–Queisser limit *IEEE J. Photovolt.* **2** 303–11
[19] Green M A and Ho-Baillie A W Y 2019 Pushing to the limit: radiative efficiencies of recent mainstream and emerging solar cells *ACS Energy Lett.* 1639–44
[20] Nayak P K, Mahek S, Snaith H J and Cahen D 2019 Photovoltaic solar cell technologies: analysing the state of the art *Nat. Rev. Mater.* **4** 269–85
[21] Guillemoles J F, Kirchartz T, Cahen D and Rau U 2019 Guide for the perplexed to the Shockley–Queisser model for solar cells *Nat. Photon.* **13** 501–5
[22] Hanifi D A *et al* 2019 Redefining near-unity luminescence in quantum dots with photothermal threshold quantum yield *Science* **363** 1199
[23] deQuilettes D W, Frohna K, Emin D, Kirchartz T, Bulovic V, Ginger D S and Stranks S D 2019 Charge-carrier recombination in Halide Perovskites *Chem. Rev.* **119** 11007–19
[24] Egger D A, Bera A, Cahen D, Hodes G, Kirchartz T, Kronik L, Lovrincic R, Rappe A M, Reichman D R and Yaffe O 2018 What remains unexplained about the properties of halide perovskites? *Adv. Mater.* **30** 1800691
[25] deQuilettes D W, Zhang W, Burlakov V M, Graham D J, Leijtens T, Osherov A, Bulovic V, Snaith H J, Ginger D S and Stranks S D 2016 Photo-induced halide redistribution in organic–inorganic perovskite films *Nat. Commun.* **7** 11683
[26] deQuilettes D W, Vorpahl S M, Stranks S D, Nagaoka H, Eperon G E, Ziffer M E, Snaith H J and Ginger D S 2015 Impact of microstructure on local carrier lifetime in perovskite solar cells *Science* **348** 683–6
[27] Leblebici S Y *et al* 2016 Facet-dependent photovoltaic efficiency variations in single grains of hybrid halide-perovskite *Nat. Energy* **1** 16093
[28] Bi Y, Hutter E M, Fang Y, Dong Q, Huang J and Savenije T J 2016 Charge carrier lifetimes exceeding 15 μs in methylammonium lead iodide single crystals *J. Phys. Chem. Lett.* **7** 923–8
[29] Fang H H, Adjokatse S, Wei H, Yang J, Blake G R, Huang J, Even J and Loi M A 2016 Ultrahigh sensitivity of methylammonium lead tribromide perovskite single crystals to environmental gases *Sci. Adv.* **2** e1600534
[30] Yang Y, Yan Y, Yang M, Choi S, Zhu K, Luther J M and Beard M C 2015 Low surface recombination velocity in solution-grown $CH_3NH_3PbBr_3$ perovskite single crystal *Nat. Commun.* **6** 7961
[31] Wenger B, Nayak P K, Wen X, Kesava S V, Noel N K and Snaith H J 2017 Consolidation of the optoelectronic properties of $CH_3NH_3PbBr_3$ perovskite single crystals *Nat. Commun.* **8** 590
[32] Dong Q, Fang Y, Shao Y, Mulligan P, Qiu J, Cao L and Huang J 2015 Electron-hole diffusion lengths >175 μm in solution-grown $CH_3NH_3PbI_3$ single crystals *Science* **347** 967
[33] Wei H, DeSantis D, Wei W, Deng Y, Guo D, Savenije T J, Cao L and Huang J 2017 Dopant compensation in alloyed $CH_3NH_3PbBr_{3-x}Cl_x$ perovskite single crystals for gamma-ray spectroscopy *Nat. Mater.* **16** 826
[34] Wei H *et al* 2016 Sensitive x-ray detectors made of methylammonium lead tribromide perovskite single crystals *Nat. Photon.* **10** 333
[35] Wei W *et al* 2017 Monolithic integration of hybrid perovskite single crystals with heterogenous substrate for highly sensitive x-ray imaging *Nat. Photon.* **11** 315
[36] Fang Y, Dong Q, Shao Y, Yuan Y and Huang J 2015 Highly narrowband perovskite single-crystal photodetectors enabled by surface-charge recombination *Nat. Photon.* **9** 679
[37] Chen Z *et al* 2017 Thin single crystal perovskite solar cells to harvest below-bandgap light absorption *Nat. Commun.* **8** 1890
[38] Chen Z, Turedi B, Alsalloum A Y, Yang C, Zheng X, Gereige I, AlSaggaf A, Mohammed O F and Bakr O M 2019 Single-crystal $MAPbI_3$ Perovskite solar cells exceeding 21% power conversion efficiency *ACS Energy Lett.* **4** 1258–9
[39] Asbeck P 1977 Self-absorption effects on radiative lifetime in GaAs–GaAlAs double heterostructures *J. Appl. Phys.* **48** 820–2
[40] Brenes R, Laitz M, Jean J, deQuilettes D W and Bulovic V 2019 Benefit from photon recycling at the maximum-power point of state-of-the-art Perovskite solar cells *Phys. Rev. Appl.* **12** 014017
[41] Rau U, Paetzold U W and Kirchartz T 2014 Thermodynamics of light management in photovoltaic devices *Phys. Rev.* B **90** 035211
[42] Staub F, Hempel H, Hebig J C, Mock J, Paetzold U W, Rau U, Unold T and Kirchartz T 2016 Beyond bulk lifetimes: insights into lead halide perovskite films from time-resolved photoluminescence *Phys. Rev. Appl.* **6** 044017
[43] Crothers T W, Milot R L, Patel J B, Parrott E S, Schlipf J, Müller-Buschbaum P, Johnston M B and Herz L M 2017 Photon reabsorption masks intrinsic bimolecular charge-carrier recombination in $CH_3NH_3PbI_3$ perovskite *Nano Lett.* **17** 5782–9
[44] Pazos-Outon L M *et al* 2016 Photon recycling in lead iodide perovskite solar cells *Science* **351** 1430–3
[45] Bercegol A, Ory D, Suchet D, Cacovich S, Fournier O, Rousset J and Lombez L 2019 Quantitative optical assessment of photonic and electronic properties in halide perovskite *Nat. Commun.* **10** 1586
[46] Ansari-Rad M and Bisquert J 2018 Insight into photon recycling in perovskite semiconductors from the concept of photon diffusion *Phys. Rev. Appl.* **10** 034062
[47] Kirchartz T, Staub F and Rau U 2016 Impact of photon recycling on the open-circuit voltage of metal halide perovskite solar cells *ACS Energy Lett.* **1** 731–9

[48] Staub F, Kirchartz T, Bittkau K and Rau U 2017 Manipulating the net radiative recombination rate in lead halide perovskite films by modification of light outcoupling *J. Phys. Chem. Lett.* **8** 5084–90
[49] Pazos-Outon L M, Xiao T P and Yablonovitch E 2018 Fundamental efficiency limit of lead iodide Perovskite solar cells *J. Phys. Chem. Lett.* **9** 1703–11
[50] Kirchartz T 2019 Photon management in perovskite solar cells *J. Phys. Chem. Lett.* **10** 5892–6
[51] Fang Y, Wei H, Dong Q and Huang J 2017 Quantification of re-absorption and re-emission processes to determine photon recycling efficiency in perovskite single crystals *Nat. Commun.* **8** 14417
[52] Gan Z, Wen X, Chen W, Zhou C, Yang S, Cao G, Ghiggino K P, Zhang H and Jia B 2019 The dominant energy transport pathway in halide perovskites: photon recycling or carrier diffusion? *Adv. Energy Mater.* **9** 1900185
[53] Mattheis J, Werner J H and Rau U 2008 Finite mobility effects on the radiative efficiency limit of pn-junction solar cells *Phys. Rev.* B **77** 085203
[54] Mattheis J 2008 Mobility and homogeneity effects on the power conversion efficiency of solar cells *Dissertation* Universität Stuttgart p 140
[55] van Roosbroeck W and Shockley W 1954 Photon-radiative recombination of electrons and holes in germanium *Phys. Rev.* **94** 1558–60
[56] Würfel P 1982 The chemical-potential of radiation *J. Phys. C: Solid State Phys.* **15** 3967–85
[57] Im J H, Lee C R, Lee J W, Park S W and Park N G 2011 6.5% efficient perovskite quantum-dot-sensitized solar cell *Nanoscale* **3** 4088–93